A Correction Algorithm for Propeller-Induced Airflow and Flight Attitude Changes during Three-Dimensional Wind Speed Measurements Made from A Rotary Unmanned Aerial Vehicle

Yanrong Yang[a+], Yuheng Zhang[a+], Tianran Han[a], Conghui Xie[a], Yayong Liu[a], Yufei Huang[a], Jietao Zhou[a], Haijiong Sun[a], Delong Zhao[b], Kui Zhang[c], Shao-Meng Li[a*]

[a] College of Environmental Sciences and Engineering, Peking University, Beijing 100871, China

[b] Beijing Key Laboratory of Cloud, Precipitation and Atmospheric Water Resources, Beijing Meteorological Service, Beijing, China

[c] Beijing Wisdominc Technology Co., Ltd, Beijing, China.

[+] Contributed equally to the work

Correspondence to: Shao-Meng Li (shaomeng.li@pku.edu.cn)

Keywords: UAV; Propeller Disturbance; Three-dimensional Wind; Correction Algorithm

Abstract

A hexa-copter unmanned aerial vehicle (UAV) was fitted with a 3-dimensional sonic anemometer to measure 3-dimensional wind speed, air temperature, relative humidity, and pressure. To obtain accurate results for 3-D wind speeds, we developed an algorithm to correct biases caused by the propeller-induced airflow disturbance, UVA movement, and changes in flight attitude in the three-dimensional wind measurements. The wind measurement platform was built based on a custom-designed

integration kit that couples seamlessly to the UAV, equipped with a payload and the sonic anemometer. Based on an accurate digital model of the integrated UVA-payload-anemometer platform, computational fluid dynamics (CFD) simulations were performed to quantify the wind speed disturbances caused by the rotation of the UAV's rotor on the anemometer during the UAV's steady flight under headwind, tailwind, and crosswind conditions. Through analysis of the simulated data, regression equations were developed to predict the wind speed disturbance, and the correction algorithm for rotor disturbances, motions, and attitude changes was developed. To validate the correction algorithm, we conducted a comparison study in which the integrated UAV system flew around a meteorological tower on which 3-D wind measurements were made at multiple altitudes. The comparison between the corrected UAV wind data and those from the meteorological tower demonstrated an excellent agreement. The corrections result in significant reductions in wind speed bias caused mostly by the propellers, along with notable changes in the dominant wind direction and wind speed in the original data. The algorithm enables reliable and accurate wind speed measurements in the atmospheric boundary layer made from rotorcraft UAV.

1.Introduction

Wind measurement is crucial in various fields of research and application, including meteorology and environmental sciences. Accurate wind characteristics facilitate modeling of atmospheric transport patterns[1, 2], remote sensing data verification[3], model input data assimilation[4, 5] and digital modeling result

optimization[6, 7]. In particular, wind profile measurements near surface can improve the understanding of atmospheric boundary layer (ABL) dynamics and micrometeorological turbulence at the surface[8], allowing detailed understandings and model description of energy and mass exchanges between air and surfaces and transport processes.

The recent development of unmanned aerial vehicles (UAVs) has provided an opportunity for the measurement of wind fields in three dimensions with high spatial resolutions[9-11]. The small size, low flight altitude, high mobility and ability to assemble sensing devices make UAVs ideal platforms from which to measure wind in the ABL[12, 13]. Multi-rotor UAVs allow flexible control of flight attitude and stationary hovering, and can carry varying payloads depending on the number of rotors[14-16], offering significant advantages in capturing high-resolution wind characteristics in low-altitude conditions[9, 17].

UAVs are often employed to measure wind characteristics both directly and indirectly. Indirect measurement methods involve utilizing pre-installed sensors on the UAV[18], in conjunction with specialized flight patterns, wind retrieval algorithm[19-21] to achieve wind speed measurement. Although this method is straightforward to operate, it does not accurately reflect actual wind conditions during flight. Direct measurement methods entail installing additional wind sensors on the UAV to obtain real-time wind information in the field. Multi-hole-probes[22, 23], pitot tubes[24, 25], and anemometers[26, 27] are commonly used sensors. Sonic anemometers are a more prevalent choice for rotorcraft UAVs, capable of measuring wind speed by detecting changes in the speed

of sound travel between different sensors[28]. Due to the increasing use of rotorcraft UAV for wind measurements, sonic anemometers are recognized as one of the most promising methods in terms of measurement accuracy and precision.

Sonic anemometers have been mounted onto rotary-wing UAV for measuring wind speed to varying degrees of success. Typically, an anemometer is mounted at a position along the central axis above the UAV, with data adjusted for the additional wind speed signals induced by UAV motion and attitude changes. Nevertheless, the strong air flow perturbations by the rotating propellers can distort real wind flow patterns and significantly affect the wind measurement accuracy[29]. Such distortions were not included in these adjustment algorithms. To address this issue, researchers have developed several new correction methods. The first method involves mounting the anemometer along the central axis high above the UAV where the rotor wash effects are believed to be limited on the wind speed measurement[30, 31]. However, it may not be suitable for hexa-copters and octocopters due to the high position required, which may raise safety and flight control concerns. The second method involves new corrections based on experiments in an indoor area to measure wind velocity signal bias caused by the rotors during flight and then subtracting the bias[32]. However, this method is limited by the indoor area's size, insufficient for full simulations of real UAV rotor speed and attitude changes during flight and inadequate for development of a comprehensive correction scheme. It also does not take into account the detailed coupling of true winds with propeller downwash. The third method is similar to the second except the use of wind tunnels to establish a more accurate relationship between

increased air speed and UAV motion or attitude parameters[12, 33]. While effective in determining numerical relationships, the method is limited by the high cost of wind tunnel experiments and more importantly the additional errors introduced by reflected airflows from the wind tunnel walls and ground and the same issues of full simulations of real UAV rotor speed and attitude changes during flight.

The flaws of these correction methods may be addressed with computational fluid dynamic (CFD) simulations of the air flows by the propellers of an UAV. To the best of our knowledge, CFD has been used to analyze airflow patterns around drones, but not for correcting wind measurements made from UAVs[34, 35]. In this paper, we present a three-dimensional wind speed correction algorithm for sonic anemometer wind measurements made from a rotary UAV that accounts for the propeller-induced airflow of the UAV based on CFD simulations, as well as the UAV motion and attitude changes during flight. The accuracy of the algorithm is verified by comparing the corrected wind speeds with wind speeds measured from a meteorological tower at multiple altitudes. Such results can contribute to ongoing efforts to improve the performance and reliability of UAV-based wind speed measurement techniques, and pave the way for its applications such as quantifying pollutant emissions from industrial complex[36].

2.Method

2.1 Equipment and Digital Model Representation

A six-rotor UAV (KWT-X6L-15, ALLTECH, China), equipped with six 32-cm diameter propellers driven by M10 KV100 brushless DC motors, was the platform from

which wind was measured. The UAV has a symmetrical motor wheelbase of 1765 mm with an unloaded takeoff weight of 22.5 kg and a maximum flight speed of 18 m/s. It has a flight endurance >30 min while carrying its maximum payload of 15 kg.

A miniature three-dimensional ultrasonic anemometer (Trisonica-Mini Wind and Weather Sensor, Anemoment, America) allowed the measurement of wind speed under 15 m/s with an accuracy of ± 0.1m/s and a resolution of 0.1 m/s, and wind direction of 0-360° with an accuracy of ± 0.1° and a resolution of 0.1°. It was set at 70 cm above the plane of the propellers of the UAV, mounted on a custom-design carbon fiber tube and frame which was further mounted onto a rectangular carbon fiber support base attached to the underbelly of the UAV body, to minimize the effect of propellers-induced flow on the anemometer measurement. The x_t-y_t-z_t coordinate axes of the anemometer, with its center as the origin, were set to be parallel to the x-y-z axes of the aircraft body frame. The mounting of the 3-D anemometer is shown in Fig. 1(a).

A base digital model of the UAV was provided by its manufacturer for the present CFD simulations. The digital model was further augmented with the accurate digital representation of the 3-D anemometer and its mounting frame. Furthermore, considering that the UAV wind measurements are usually tied to other air measurement applications, necessitating additional payload attached to the UAV underbelly simultaneously. Such a payload on the UAV needs also to be included in the digital model for the CFD simulation. In the present case, we added the digital model of a 6.37 kg air sampler developed in our group[36] to the UAV base digital model (Fig. 1(b)).

For CFD simulations, the complete digital model for the UAV and its payloads

was set in the x_s-y_s-z_s simulation coordinate system in Solidworks, a computational fluid simulation tool, on a one-to-one scale (Fig. 1(b)).

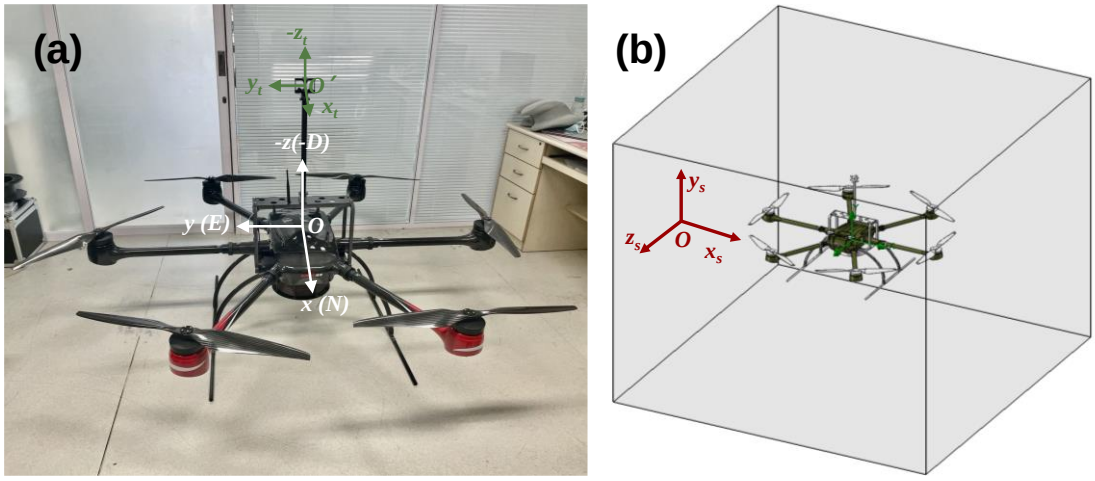

Figure 1. (a) The UAV wind speed measurement platform. (b) The digital model of the UAV wind measurement platform in the 3D CFD model simulation domain.

2.2 CFD Simulation Parameters Configuration

2.2.1 Environmental Parameters

Since the UAV's predominant flights are within the atmospheric boundary layer, characterized by significant variability in wind speed and directions, a flight envelope for the UAV in the simulated environments was setup for the complete UAV digital model for flight altitudes of 30 meters and 1000 meters, respectively. These flight envelopes were designed for the UAV to subject to headwind, tailwind, and crosswind relative to its flight direction. Under the constraint that the UAV can only operate under true wind speeds ≤18 m/s, and assuming the applicability of the correction algorithm to most flight scenarios, CFD simulations were conducted for the UAV under these three wind directions. The simulations encompassed the following flight envelopes as listed

in Table 1: the UAV flew at ground speeds of 18, 14, 10, and 8 m/s, respectively, and adapted to wind speeds of 1.5, 3.3, 5.4, 7.9, 10.7, and 14 m/s.

Table 1. Ground speed and wind speed configuration in the presence of tailwind, headwind, and crosswind conditions relative to the UAV's flight direction.

Wind direction	Ground Speed (m/s)	Wind speed (m/s)	Wind direction	Ground Speed (m/s)	Wind speed (m/s)	Wind direction	Ground Speed (m/s)	Wind speed (m/s)
Tailwind	8	1.5	Headwind	8	1.5	Crosswind	8	1.5
		3.3			3.3			3.3
		5.4			5.4			5.4
		7.9						7.9
		10.7						10.7
								14
	10	1.5		10	1.5		10	1.5
		3.3			3.3			3.3
		5.4			5.4			5.4
		7.9			7.9			7.9
		10.7						10.7
								14
	14	1.5		14	1.5		14	1.5
		3.3			3.3			3.3
		5.4			5.4			5.4
		7.9			7.9			7.9
		10.7			10.7			10.7
								14
	18	1.5		18	1.5		18	1.5
		3.3			3.3			3.3
					5.4			5.4
					7.9			7.9
					10.7			10.7
					14			14

2.3 Flight Parameters

The movements of the UAV through air, including takeoff, ascent/descent, attitude changes, turning, and horizontal flights, are driven by the rotary propellers, whose

power requirement is closely tied to the weights of the UAV and its payload as well as the relative motions of the UAV in air. During a normal flight, the UAV adjusts its inclination angle and propeller speeds in order to achieve a set ground speed for flight. By analyzing the gravity G, pull T and wind resistance D experienced by the UAV under flight conditions, its inclination angle θ and propeller rotation speed M can be calculated according to Eqs. (1)-(5)[37].

$$tan\,\theta \times mg = D \tag{1}$$

$$p \times (sin\theta \times S_{xoy} + cos\theta \times S_{xoz}) = D \tag{2}$$

$$0.5\rho(V_{wind} + V_{UAV})^2 = p \tag{3}$$

$$cos\,\theta \times mg = T \tag{4}$$

$$T = C_T \times \rho \times \left(\frac{M}{60}\right)^2 \times D_p^{\,4} \tag{5}$$

where θ is the inclination angle of the UAV; m is the combined weight of the UAV and the payloads (i.e, the air sampler and the anemometer plus its installation frame in the present case), calculated to be 28.869 kg; g is the gravitational constant at 9.8 m/s^2; D is the wind resistance in Newtons; V_{wind} is the wind speed in m/s; V_{UAV} is the ground speed of the UAV in m/s; p is the wind pressure on the UAV in N/m^2; S_{xoy} and S_{xoz} are the projected surfaces of the UAV in the horizontal direction and vertical directions, determined to be 0.296 and 0.229 m^2, respectively; C_T is the rotor pull coefficient with an experimentally determined value of 0.048542; D_p is the UAV propeller diameter at 0.8128 m; ρ is the air density in kg/m^3; T is each rotor pull in Newton; M is the rotation speed of the rotors in RPM.

The calculated M values were corrected for the different UAV attitude, V_{wind}, and V_{UAV} combinations as appropriate. Each set of flight condition parameters that

constitute the full flight envelope, including wind directions, wind speeds, airspeeds, ground speed, inclination, wind resistance, pull, *M* and corrected *M* are given in Table S1 and S2 of Support Information. The CFD simulations were performed to determine the wind fields for each set of parameters in the flight envelope one at a time.

2.4 Simulation Parameters

During the CFD flow simulations of the UAV using Solidworks, the computational domain was set to 3.3×3.3×3.3 m^3 according to the wingspan of the UAV, with the complete UAV plus payload digital model set at the center of the domain. The computational domain was divided into two parts with different spatial resolutions based on the grid sizes，considering the computational time and accuracy required for resolving the details of the digital UAV model. The first part was the global domain with a grid size of 0.23×0.23×0.23 m^3, providing a lower spatial resolution. The second part was a nested subdomain within the global domain, specifically defined for the position and dimensions of the anemometer to simulate the measured velocities. The grid size for this nested subdomain was set at 0.0125×0.0125×0.0125 m^3, providing a higher spatial resolution. The total number of grids in the computational domain was 1.113×10^8, and the specific grid configurations are shown in the Fig. 2. The fluid was modeled as air with characteristics of turbulent and laminar flow, with a turbulence intensity of 0.1% and a turbulence length scale of 0.012 m. The atmospheric pressure was adjusted to 100976.99 Pa and 90017.95 Pa at altitudes of 30 m and 1000 m, respectively, and the atmospheric temperature was assumed to be 25 °C at both altitudes.

The relative humidity at different altitudes was determined based on the prescribed pressure and temperature corresponding to each altitude. The UAV's airspeed and aerodynamic angles, including the angle of attack and sideslip, were configured according to the different flight parameters provided in Table S1 and S2. To represent the rotor digitally, six virtual cylinders of the same volume were used to encapsulate the six rotors, with their circumferences match the rotating trajectory of the propeller tip. These virtual cylinders were treated as the rotational regions in the CFD simulation, with their rotation directions aligned with the actual rotation direction of the UAV's propellers. The rotation direction from rotor No. 1 to 6 was alternately clockwise and counterclockwise, and the rotation speed for each flight condition was obtained from Table S1 and S2.

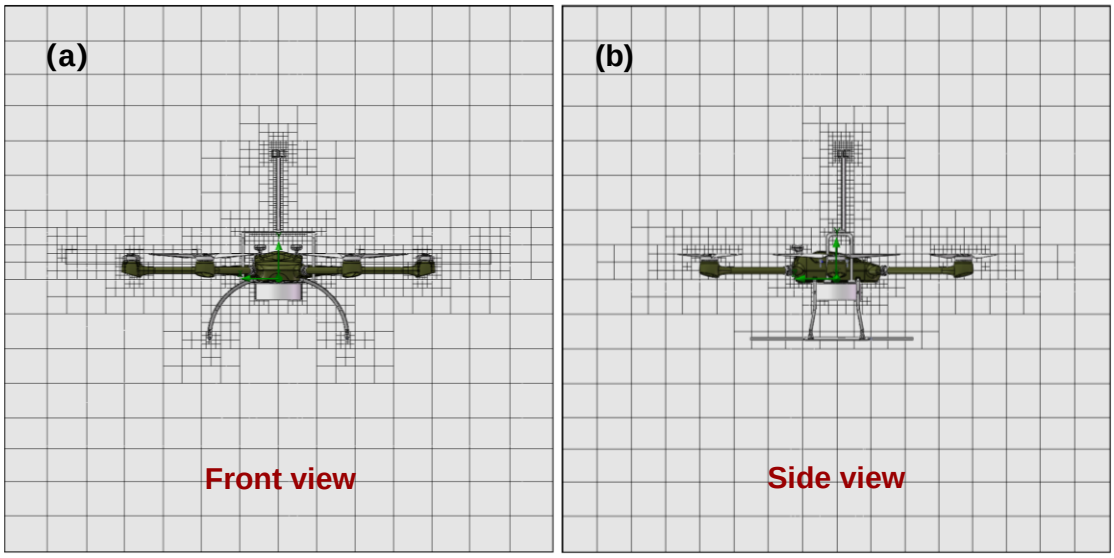

Figure 2. Grid configuration of the computational domain.

To ensure relatively accurate simulations, two categories of flow field properties were specified as computational objectives prior to the start of the simulations, and the simulations were terminated upon convergence of the simulation results for all

objectives. The first category comprised global domain computational objectives, including average total pressure (PG), average velocity (VG), average vertical velocity (VGy), and average forward velocity (VGz), where the subscript G denotes the global domain. The second category consisted of subdomain computational objectives, which included the average velocity (Vs), three-dimensional average speed components Vsx, Vsy, and Vsz at the anemometer position in the simulation coordinate system.

Upon simulation completion, these velocity components (Vs_x, Vs_y, Vs_z) were further converted to velocity components at the anemometer sensor position (u_{x_sensor}, u_{y_sensor}, u_{z_sensor}) in the airframe coordinate according to Eqs. (6)-(8) below. The converted velocities, u_{x_sensor}, u_{y_sensor}, u_{z_sensor}, were subtracted from the wind velocity (denoted as u_{x_air}, u_{y_air}, and u_{z_air}) setting for each CFD simulation, to estimate the false wind signals arising from the induced flow by the UAV rotors, expressed with Δu_x, Δu_y and Δu_z, respectively, using Eqs. (9)-(11).

$$u_{x\_sensor} = -Vs_z \tag{6}$$

$$u_{y\_sensor} = Vs_x \tag{7}$$

$$u_{z\_sensor} = -Vs_y \tag{8}$$

$$\Delta u_x = u_{x\_sensor} - u_{x\_air} \tag{9}$$

$$\Delta u_y = u_{y\_sensor} - u_{y\_air} \tag{10}$$

$$\Delta u_z = u_{z\_sensor} - u_{z\_air} \tag{11}$$

In other words, the false wind signals Δu_x, Δu_y and Δu_z are the terms that must be determined and corrected for in the wind measurements from the UAV.

3.Result and Discussion

3.1 The effect of flight altitude on rotor interference with anemometer measurements

Through simulating the flight of UAV in diverse environmental scenarios (as illustrated by the example results in Fig. S1), the deceptive signals produced by the rotors of the UAVs on the anemometer at different altitudes and wind characteristics were captured. Initially, the influence of flight altitude on the false signals was examined.

The simulation results for the UAV anemometer under different wind directions and speeds at the 30 m and 1000 m altitudes are summarized in Table S3 and S4, respectively. The simulated flight data under tailwind and headwind conditions were integrated into a unified data set since the UAV flight velocity vector is parallel to the tailwind and headwind velocity vectors during normal flight. The simulated false wind signals on the anemometer in the airframe x, y, and z directions, caused by the propeller induced airflow under tailwind and headwind conditions, were represented by $\Delta u_x^{T/HW}$, $\Delta u_y^{T/HW}$, and $\Delta u_z^{T/HW}$, respectively. For the tailwind and headwind datasets, according to the Wilcoxon non-parametric test for paired samples (as shown in Table 2), the differences in $\Delta u_x^{T/HW}$, $\Delta u_y^{T/HW}$ and $\Delta u_z^{T/HW}$ were not significant (Sig. = 0.05) at either the 30 m or the 1000 m altitudes. Therefore, in the presence of tailwind or headwind, the interference from the UAV propeller-induced flow on the anemometer measurement can be considered independent of the flight altitude in this altitude range.

Similarly, the simulated false wind signals on the anemometer in the x, y, and z directions were represented by Δu_x^{CW}, Δu_y^{CW}, and Δu_z^{CW}. The Wilcoxon non-parametric test of paired samples was also applied (shown in Table 1) between the two altitudes. No significant differences were found for Δu_x^{CW}, Δu_z^{CW} between the two

altitudes, but there was an obvious discrepancy for Δu_y^{CW} （$p=1.5\times10^{-5}<\alpha=0.05$）at the two altitudes. This indicates that under cross wind conditions, the disturbances of the UAV propeller in the x and z directions of the anemometer are not altitude dependent, but that in the y (upward) direction it is necessary to distinguish the altitude.

Table 2. Wilcoxon nonparametric tests for paired samples of false wind velocity signals between 30 m and 1000 m flight altitudes

Types of wind	False Wind Signal	Significance	α	Test results
Tailwind/Headwind	$\Delta u_x^{T/HW}$	0.93	0.05	No difference
	$\Delta u_y^{T/HW}$	0.72	0.05	No difference
	$\Delta u_z^{T/HW}$	0.21	0.05	No difference
Crosswind	Δu_x^{CW}	0.36	0.05	No difference
	Δu_y^{CW}	1.5×10^{-5}	0.05	Significant difference
	Δu_z^{CW}	0.81	0.05	No difference

3.2 Rotor Interference on Anemometer Measurements

The false wind signals ($\Delta u_x^{T/HW}$, $\Delta u_y^{T/HW}$, and $\Delta u_z^{T/HW}$) on the anemometer resulting from the UAV rotor -induced flows under tailwind and headwind conditions at both flight altitudes were aggregated and fitted as dependent variables in a regression using u_{x_sensor} as the independent variable as shown in Fig. 3. Good linear relationships $y=0.51+0.061x$ (R^2=0.75), $y=-0.010+0.70x$ (R^2=0.69) and $y=1.22+0.17x$ (R^2=0.95) were found between $\Delta u_x^{T/HW}$, $\Delta u_y^{T/HW}$, and $\Delta u_z^{T/HW}$ and the simulated velocity components in the x-direction (u_{x_sensor}), respectively. Thus, using the UAV velocity components in x direction, the false wind signals caused by the UAV propellers

can be determined and removed from the raw measured wind velocity from the anemometer.

For crosswind conditions, regressions were fitted with false wind signals (Δu_x and Δu_z) as dependent variables and u_{x_sensor} as the independent variable in the same way (See Fig. 4). A linear relationship was observed between the false wind signals in both x and z directions (Δu_x^{CW} and Δu_z^{CW}) and u_{x_sensor}, with the specific expressions $y = 0.71 + 0.071x$ ($R^2 = 0.65$) and $y = 0.84 + 0.13x$ ($R^2 = 0.86$), respectively. As described in Section 3.1, Δu_y^{CW} was sensitive to flight altitude under crosswind conditions, hence Δu_y^{CW} at 30 m and 1000 m altitude ($\Delta u_{y(30)}^{CW}$ and $\Delta u_{y(1000)}^{CW}$) were regressed against u_{y_sensor} for the two flight altitudes separately. The $\Delta u_{y(30)}^{CW}$ exhibited a linear relationship with u_{y_sensor} ($y=-0.0043+0.19x$, $R^2=0.45$). However, the correlation coefficient between $\Delta u_{y(1000)}^{CW}$ and u_{y_sensor} was found to be lower than 0.5, indicating that $\Delta u_{y(1000)}^{CW}$ may be considered independent of u_{y_sensor}. Therefore, the average value of $\Delta u_{y(1000)}^{CW}$ (0.006 m/s) was regarded as the $\Delta u_{y(1000)}^{CW}$ at this flight altitude.

Despite the dependence of Δu_y^{CW} on flight altitudes, $\Delta u_{y(30)}^{CW}$ and $\Delta u_{y(1000)}^{CW}$ are confined to a similar numeric range. Therefore, they may be roughly considered as representing Δu_y for lower altitude (e.g., 0-500 m) and higher altitude (e.g., 500-1000 m), respectively.

Hence, for crosswind situations, the wind velocities in the x, y and z directions measured by the anemometer are corrected by subtracting Δu_x^{CW}, Δu_z^{CW} and $\Delta u_{y(0-500)}^{CW}$ which are estimated from $u_{x\_sensor}/u_{y\_sensor}$, or at relatively high flight altitudes using

a constant value of 0.006 m/s for $\Delta u_{y(501-1000)}^{CW}$.

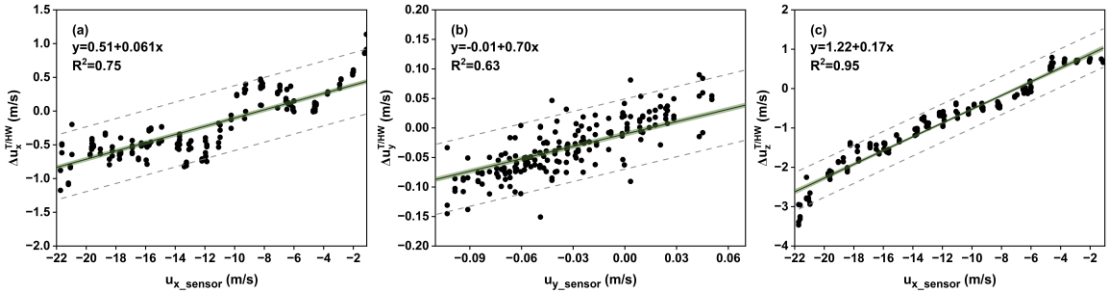

Figure 3. Regression fit of artificial velocity ($\Delta u_x^{T/HW}$, $\Delta u_y^{T/HW}$ and $\Delta u_z^{T/HW}$) with u_{x_sensor} for tailwind and headwind flight conditions at two altitudes. In the figure, simulation data are marked with black dots, fitted curves are indicated in black lines, the 95% confidence bands are identified as green shadows, and the 95% prediction bands are represented with gray dashed area.

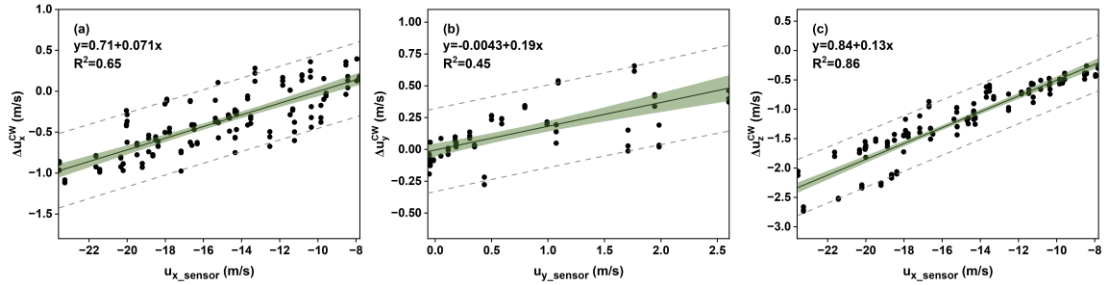

Figure 4. Regression fit of false wind velocity signals Δu_x^{CW}, Δu_z^{CW} and $\Delta u_{y(0-500)}^{CW}$ with $u_{x\_sensor}/u_{y\_sensor}$ for crosswind flight conditions at two altitudes. The symbols in the figure are the same as in Figure 3.

3.3 The Overall Correction Algorithm

3.3.1 Motion and Attitude Compensation Correction of UAV

In addition to the false wind signals caused by propeller rotations, additional false wind velocity signals from the anemometer can be attributed to UAV movement and attitude (pitch, roll and yaw) changes during flight, and as such also need correction. When the UAV moves horizontally and vertically relative to the ground, the velocity vector measured by the anemometer is a vector combination of the true wind velocity and the UAV's ground velocity. Consequently, the ground velocity of the UAV (v_x and v_z, with v_y always 0 due to no motion in the y direction) contributes false wind velocity

components to measurements by the anemometer. Moreover, the UAV's flight attitude undergoes adjustments in the pitch, roll, and yaw Euler angles (θ, φ, and ψ, respectively), in order to compensate for aerodynamic resistance or adapt to flight plans. These adjustments lead to the anemometer measuring additional velocities resulting from the rotational rates of the attitude angles ($\mu(\theta)$ and $\mu(\varphi)$, with $\mu(\psi)$ remaining zero due to the alignment of the rotational axis of ψ with the line connecting the UAV's center of gravity and the anemometer. Furthermore, the effect is further amplified by the distance (r) between the anemometer and the UAV's center of gravity. It is noteworthy that there is currently no reported correction algorithm for influence of attitude angle variations on anemometer wind velocity measurements from UAVs. To obtain accurate wind information, after eliminating the aforementioned interferences, the wind velocities (u_x, u_y and u_z) observed by the anemometer in the airframe coordinate (x, y and z directions) were transformed to the North-East-Down (NED) ground coordinate using the direction cosine matrix (DCM) as given in Eq. (12).

$$\begin{bmatrix} u_N \\ u_E \\ u_D \end{bmatrix} = \mathrm{DCM}(\theta, \varphi, \psi)\left(\begin{bmatrix} u_x \\ u_y \\ u_z \end{bmatrix} + \begin{bmatrix} v_x \\ 0 \\ -v_z \end{bmatrix} + \begin{bmatrix} \mu(\theta) \\ -\mu(\varphi) \\ 0 \end{bmatrix}\right) \tag{12}$$

$$\mathrm{DCM}(\theta, \varphi, \psi) = \begin{bmatrix} \cos(\psi) & -\sin(\psi) & 0 \\ \sin(\psi) & \cos(\psi) & 0 \\ 0 & 0 & 1 \end{bmatrix}\begin{bmatrix} \cos(\theta) & 0 & \sin(\theta) \\ 0 & 1 & 0 \\ -\sin(\theta) & 0 & \cos(\theta) \end{bmatrix}\begin{bmatrix} 1 & 0 & 0 \\ 0 & \cos(\varphi) & -\sin(\varphi) \\ 0 & \sin(\varphi) & \cos(\varphi) \end{bmatrix} \tag{13}$$

where DCM is defined by Eq. (13); u_N, u_E and u_D refer to corrected North, East and Down components of wind velocity in the ground coordinate; v_x and v_z are the motion velocities of the UAV in the x and z directions respectively, which are directly provided by the GPS receiver output of the UAV or can be directly computed from the longitude/latitude coordinate outupt; $\mu(\theta)$ and $\mu(\varphi)$ represent the product of the pitch rate ω (θ) and roll rate ω (φ), respectively, with the rotation radius r, which is

the distance between the anemometer and the center of gravity of the UAV, as defined in Eqs. (14)-(15). Due to the alignment of the anemometer's z-axis with that of the UAV, the variation in yaw ψ does not introduce false wind speed to signals from the anemometer in the airframe coordinate, resulting in μ(ψ) being equal to zero.

$$\mu(\theta) = \omega(\theta) \times r = \frac{d(\theta)}{dt} \times r \tag{14}$$

$$\mu(\varphi) = \omega(\varphi) \times r = \frac{d(\varphi)}{dt} \times r \tag{15}$$

where $\omega(\theta)$ and $\omega(\varphi)$ are defined as the differentiation of θ and φ with respect to time *t*, respectively.

3.3.2 Compensation Correction for Induced-Flow Disturbance by UAV Rotor Propellers

Based on the statistical analyses of the fluid simulation results in Section 3.2, the regression relationships between the false wind velocity signals generated by the propeller rotation and the simulated wind components sensed by the anemometer are integrated into the motion and attitude correction algorithm of UAV given in Eq. (12). The updated wind velocity correction algorithm is given as Equation 16, whose second and third vectors on the right side of Equation 16 represent the contributions of the propeller-induced wind signals under tailwind/headwind and crosswind conditions to u_x, u_y and u_z, respectively, with A and B defined in Eqs. (17)-(18) to quantify their magnitudes. Since the measured wind velocities u_x and u_y from the anemometer correspond to the simulated u_{x_sensor} and u_{y_sensor}, respectively, the regression relationships are modified by replacing u_x and u_y with u_{x_sensor} and u_{y_sensor}, respectively. This yields the estimations of the false wind velocity signals, Δu_x, Δu_y and Δu_z, under

different wind directions, in relation to u_x and u_y, as specified by Eqs. (19)-(25). Using Eq. 16, the actual wind velocity components, including north wind (u_N), east wind (u_E), and vertical wind (u_D), are computed after correcting for the effects of UAV's rotor propeller disturbance, motion, and attitude on the wind signal measurements from the anemometer.

$$\begin{bmatrix} u_N \\ u_E \\ u_D \end{bmatrix} = \mathrm{DCM}(\theta, \varphi, \psi) \left(\begin{bmatrix} u_x \\ u_y \\ u_z \end{bmatrix} - \begin{bmatrix} \mathrm{A} \times \Delta u_x^{T/HW} \\ \mathrm{A} \times \Delta u_y^{T/HW} \\ \mathrm{A} \times \Delta u_z^{T/HW} \end{bmatrix} - \begin{bmatrix} \mathrm{B} \times \Delta u_x^{CW} \\ \mathrm{B} \times \Delta u_y^{CW} \\ \mathrm{B} \times \Delta u_z^{CW} \end{bmatrix} + \begin{bmatrix} v_x \\ 0 \\ v_z \end{bmatrix} + \begin{bmatrix} -\mu(\theta) \\ \mu(\varphi) \\ 0 \end{bmatrix} \right) \quad (16)$$

$$A = \left| \frac{u_x}{\sqrt{{u_x}^2 + {u_y}^2}} \right| \quad (17)$$

$$B = \left| \frac{u_y}{\sqrt{{u_x}^2 + {u_y}^2}} \right| \quad (18)$$

$$\Delta u_x^{T/HW} = 0.51 + 0.061 \times u_x \quad (19)$$

$$\Delta u_y^{T/HW} = -0.01 + 0.70 \times u_y \quad (20)$$

$$\Delta u_z^{T/HW} = 1.22 + 0.17 \times u_x \quad (21)$$

$$\Delta u_x^{CW} = 0.71 + 0.071 \times u_x \quad (22)$$

$$\Delta u_y^{CW} = -0.0043 + 0.19 \times u_y \quad (h = 0\sim500\ \mathrm{m}) \quad (23)$$

$$\Delta u_y^{CW} = 0.006 \quad (h = 501\sim1000\ \mathrm{m}) \quad (24)$$

$$\Delta u_z^{CW} = 0.84 + 0.13 \times u_x \quad (25)$$

In Eqs. (23)-(24), the variable h represents the flight altitude of the UAV.

3.4 Validation of the Correction Algorithm

To validate the effectiveness of the correction algorithm given by Eq. (16), wind speeds corrected for UAV motion and attitude compensation only (Eq. (12) and denoted as UAV_Original) and the wind speeds corrected for rotor disturbance, motion, and attitude compensation (Eq. (16) and denoted as UAV_Revised) were compared with 3-

dimensional winds measured on an 80-meter meteorological tower (denoted as Tower). The comparison experiment was conducted with the UAV flying wind-boxes around the meteorological tower within the Experimental Base of the Beijing Key Laboratory of Cloud, Precipitation and Atmospheric Water Resources. The meteorological tower was equipped with three-dimensional ultrasonic anemometers positioned at heights of 30, 50, and 70 m, with one sensor in the north and one in the south (see Fig. S2). The UAV flew around the tower in a box flight path at a horizontal distance of about 10 m away from the tower, at all three heights. Given the potential interference from near-surface vegetation on the 30-meter anemometer on the tower, wind velocities acquired by the UAV at 50 and 70 m heights during steady flight intervals were analyzed herein.

The results in Fig. 6(A) demonstrate that at elevated wind speeds (>3 m/s), the wind velocities of UAV_Revised were substantially lower than UAV_Original and approximated those from the Tower more closely. In contrast, under gentle wind speeds (≤3 m/s), UAV_Revised exhibited greater consistency with UAV_Original but there was still a significant down-revision in the average speed in UAV_Revised. The average wind speeds of UAV_Original, UAV_Revised, and Tower were 2.4, 1.91, and 1.81 m/s, respectively, with UAV_Revised exhibiting a 22% decrease compared to UAV_Original. The statistical analysis using the Wilcoxon signed-rank test confirmed a significant difference ($p<0.01$) in wind speed between UAV_Original and Tower, whereas no significant differences ($p>0.01$) were found between UAV_Revised and Tower (as shown in Fig.S3). Moreover, under stronger winds, the wind direction values of UAV_Revised, UAV_Original, and Tower were relatively similar, yet at weaker winds,

UAV_Revised showed a small low-bias (Fig. 5(B)). Compared to UAV_Original, UAV_Revised showed a much improved match between the corrected wind velocity and frequency distributions versus Tower (Fig. 5(C)), both showing predominant northerly winds. In summary, these analyses indicated that Eq. 16 can effectively correct wind measurement biases induced by UAV disturbances, motion, and attitude changes, particularly at higher wind speeds.

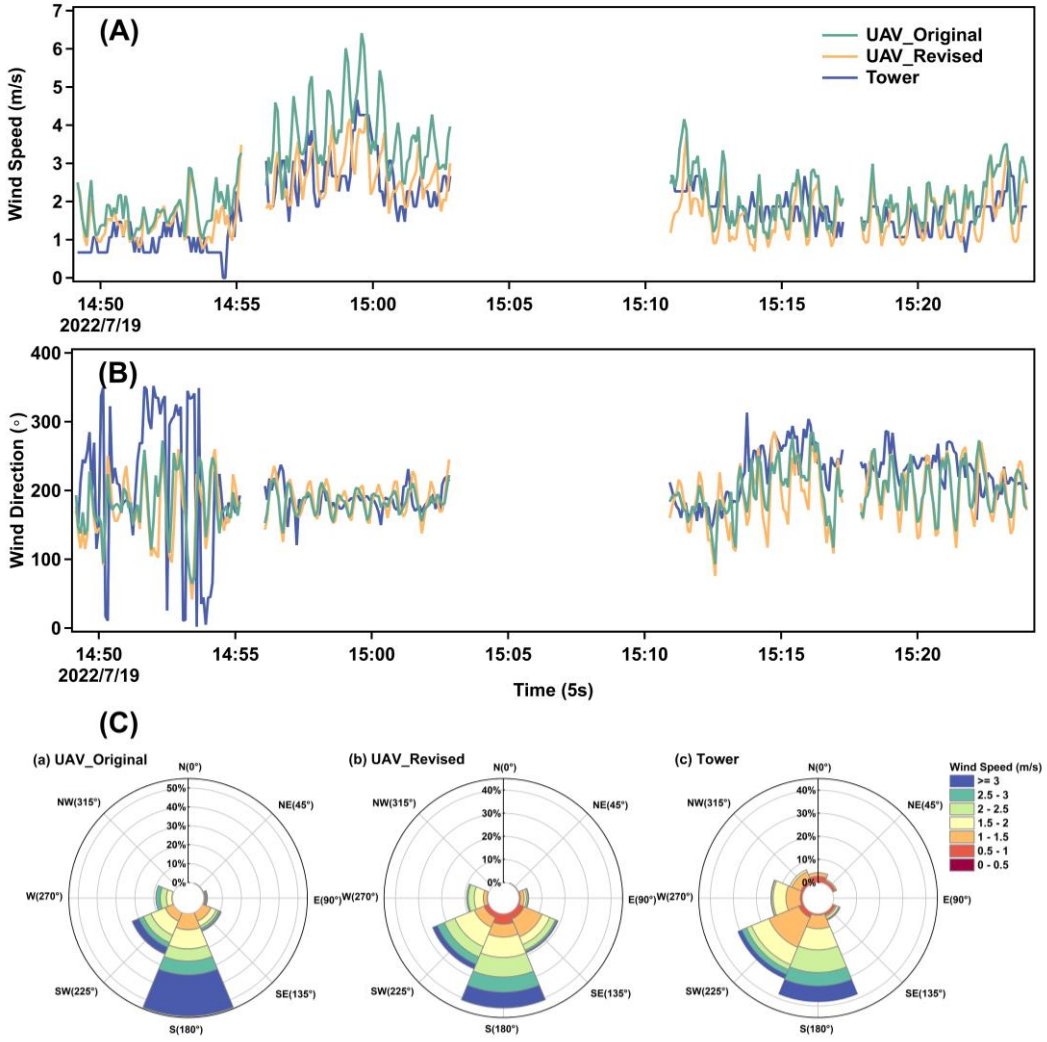

Figure 5. (A) Time-history comparison of wind speed corrected by the UAV compensation algorithm with those measured by the meteorological tower. (B) Time-history comparison of wind direction corrected by the UAV compensation algorithm with those measured by the meteorological tower. (C) Comparison of wind roses between wind corrected by the unmanned aerial vehicle compensation algorithm and those measured by the meteorological tower. (Note: The

meteorological tower measured wind data at 5 s intervals, while the UAV-based measured and corrected wind data was averaged using a 10 s sliding window before calculating 5 s mean values.)

4.Conclusions and Prospective

The scenarios involving direct measurements of wind fields within the atmospheric boundary layer using multi-rotor UAVs have become progressively commonplace, heightening the significance of accurate wind assessment. However, the rotor propellers during UAV flight introduce additional induced flows at the anemometer location, leading to false wind speed signals. For the present UAV-anemometer-payload configuration, a CFD-based method was used to simulate the process of the UAV wind measurement platform during stable flights under headwind, tailwind, and crosswind conditions. The analyses of induced airflows surrounding the anemometer led to a predictive tool for disturbance airflows. Building upon the UAV motion and attitude correction algorithm, a correction algorithm was proposed for the combined false wind signals from UAV rotor propeller disturbance, motion, and attitude changes during UAV flights. Through comparison of the corrected wind speeds derived from measurements taken from the UAV platform and concurrent three-dimensional wind measurements from a nearby meteorological tower, the validity of the correction algorithm has been demonstrated. This result presents a viable approach for directly measuring wind speeds with good accuracy from multi-rotor UAV flights. Indeed, during the first application of the UAV measurement platform to determine greenhouse gas emission rates from a large coking plant in one of the largest steelmaker in the country, we have demonstrated that the emission rates determined on the basis of

greenhouse gas concentration and 3-dimensional wind measurements match closely with emission rates determined from material balance[36], again providing a secondary validation of such a correction algorithm.

This research focused on the steady flight state of the UAV. It remains to be seen whether such a correction algorithm can be applied to scenarios during UAV ascents, descents, and hovering. Our preliminary assessment of these scenarios indicate that the correction algorithm is applicable with slightly larger biases. Nonetheless, such a topic is worthy of further study. In subsequent research, we intend to extend the investigation to encompass a broader spectrum of UAV flight states, with the objective of achieving a more precise and comprehensive correction algorithm of wind speeds directly measured during diverse flight circumstances.

Acknowledgment. This project was supported by a grant from the National Natural Science Foundation of China Creative Research Group Fund (22221004).

Reference

(1) Gryning, S. E.; Holtslag, A. A. M.; Irwin, J. S.; Sivertsen, B., Applied dispersion modeling based on meteorological scaling parameters. *Atmos. Environ.* **1987,** *21*, (1), 79-89.

(2) Stockie, J. M., The mathematics of atmospheric dispersion modeling. *Siam Rev* **2011,** *53*, (2), 349-372.

(3) Drob, D. P.; Emmert, J. T.; Meriwether, J. W.; Makela, J. J.; Doornbos, E.; Conde, M.; Hernandez, G.; Noto, J.; Zawdie, K. A.; McDonald, S. E.; Huba, J. D.; Klenzing, J. H., An update to the horizontal wind model (hwm): The quiet time thermosphere. *Earth Space Sci* **2015,** *2*, (7), 301-319.

(4) Gousseau, P.; Blocken, B.; Stathopoulos, T.; van Heijst, G. J. F., Cfd simulation of near-field pollutant dispersion on a high-resolution grid: A case study by les and rans for a building group in downtown montreal. *Atmos. Environ.* **2011,** *45*, (2), 428-438.

(5) Vardoulakis, S.; Fisher, B. E. A.; Pericleous, K.; Gonzalez-Flesca, N., Modelling air quality in street canyons: A review. *Atmos. Environ.* **2003,** *37*, (2), 155-182.

(6) Booij, N.; Ris, R. C.; Holthuijsen, L. H., A third-generation wave model for coastal regions - 1.

Model description and validation. *J Geophys Res-Oceans* **1999,** *104*, (C4), 7649-7666.
(7) van Hooff, T.; Blocken, B., Coupled urban wind flow and indoor natural ventilation modelling on a high-resolution grid: A case study for the amsterdam arena stadium. *Environ Modell Softw* **2010,** *25*, (1), 51-65.
(8) Seibert, P.; Beyrich, F.; Gryning, S. E.; Joffre, S.; Rasmussen, A.; Tercier, P., Review and intercomparison of operational methods for the determination of the mixing height. *Atmos. Environ.* **2000,** *34*, (7), 1001-1027.
(9) McGonigle, A.; Aiuppa, A.; Giudice, G.; Tamburello, G.; Hodson, A.; Gurrieri, S., Unmanned aerial vehicle measurements of volcanic carbon dioxide fluxes. *Geophys Res Lett* **2008,** *35*, (6).
(10) Martin, S.; Bange, J.; Beyrich, F., Meteorological profiling of the lower troposphere using the research uav" m 2 av carolo". *Atmos Meas Tech* **2011,** *4*, (4), 705-716.
(11) Kim, M.-S.; Kwon, B. H., Estimation of sensible heat flux and atmospheric boundary layer height using an unmanned aerial vehicle. *Atmosphere-Basel* **2019,** *10*, (7), 363.
(12) Thielicke, W.; Hubert, W.; Muller, U.; Eggert, M.; Wilhelm, P., Towards accurate and practical drone-based wind measurements with an ultrasonic anemometer. *Atmos Meas Tech* **2021,** *14*, (2), 1303-1318.
(13) Shaw, J. T.; Shah, A. D.; Yong, H.; Allen, G., Methods for quantifying methane emissions using unmanned aerial vehicles: A review. *Philos T R Soc A* **2021,** *379*, (2210).
(14) Villa, T. F.; Gonzalez, F.; Miljievic, B.; Ristovski, Z. D.; Morawska, L., An overview of small unmanned aerial vehicles for air quality measurements: Present applications and future prospectives. *Sensors-Basel* **2016,** *16*, (7).
(15) Riddell, K. D. A., *Design, testing and demonstration of a small unmanned aircraft system (suas) and payload for measuring wind speed and particulate matter in the atmospheric boundary layer*. University of Lethbridge (Canada): 2014.
(16) Bonin, T.; Chilson, P.; Zielke, B.; Klein, P.; Leeman, J., Comparison and application of wind retrieval algorithms for small unmanned aerial systems. *Geoscientific Instrumentation, Methods and Data Systems* **2013,** *2*, (2), 177-187.
(17) Anderson, K.; Gaston, K. J., Lightweight unmanned aerial vehicles will revolutionize spatial ecology. *Front Ecol Environ* **2013,** *11*, (3), 138-146.
(18) Elston, J.; Argrow, B.; Stachura, M.; Weibel, D.; Lawrence, D.; Pope, D., Overview of small fixed-wing unmanned aircraft for meteorological sampling. *J Atmos Ocean Tech* **2015,** *32*, (1), 97-115.
(19) Bonin, T. A.; Chilson, P. B.; Zielke, B. S.; Klein, P. M.; Leeman, J. R., Comparison and application of wind retrieval algorithms for small unmanned aerial systems. *Geosci Instrum Meth* **2013,** *2*, (2), 177-187.
(20) Rautenberg, A.; Graf, M. S.; Wildmann, N.; Platis, A.; Bange, J., Reviewing wind measurement approaches for fixed-wing unmanned aircraft. *Atmosphere-Basel* **2018,** *9*, (11).
(21) Gonzalez-Rocha, J.; Woolsey, C. A.; Sultan, C.; De Wekker, S. F. J., Sensing wind from quadrotor motion. *J Guid Control Dynam* **2019,** *42*, (4), 836-852.
(22) Soddell, J. R.; McGuffie, K.; Holland, G. J., Intercomparison of atmospheric soundings from the aerosonde and radiosonde. *J Appl Meteorol* **2004,** *43*, (9), 1260-1269.
(23) Spiess, T.; Bange, J.; Buschmann, M.; Vorsmann, P., First application of the meteorological mini-uav'm2av'. *Meteorologische Zeitschrift* **2007,** *16*, (2), 159-170.
(24) Niedzielski, T.; Skjøth, C.; Werner, M.; Spallek, W.; Witek, M.; Sawiński, T.; Drzeniecka-Osiadacz, A.; Korzystka-Muskała, M.; Muskała, P.; Modzel, P., Are estimates of wind characteristics based on

measurements with pitot tubes and gnss receivers mounted on consumer-grade unmanned aerial vehicles applicable in meteorological studies? *Environ Monit Assess* **2017,** *189*, 1-18.
(25) Langelaan, J. W.; Alley, N.; Neidhoefer, J., Wind field estimation for small unmanned aerial vehicles. *J Guid Control Dynam* **2011,** *34*, (4), 1016-1030.
(26) Rogers, K.; Finn, A., Three-dimensional uav-based atmospheric tomography. *J Atmos Ocean Tech* **2013,** *30*, (2), 336-344.
(27) Nolan, P. J.; Pinto, J.; Gonzalez-Rocha, J.; Jensen, A.; Vezzi, C. N.; Bailey, S. C. C.; de Boer, G.; Diehl, C.; Laurence, R.; Powers, C. W.; Foroutan, H.; Ross, S. D.; Schmale, D. G., Coordinated unmanned aircraft system (uas) and ground-based weather measurements to predict lagrangian coherent structures (lcss). *Sensors-Basel* **2018,** *18*, (12).
(28) Thielicke, W.; Hübert, W.; Müller, U.; Eggert, M.; Wilhelm, P., Towards accurate and practical drone-based wind measurements with an ultrasonic anemometer. *Atmos Meas Tech* **2021,** *14*, (2), 1303-1318.
(29) de Divitiis, N., Wind estimation on a lightweight vertical-takeoff- and-landing uninhabited vehicle. *J Aircraft* **2003,** *40*, (4), 759-767.
(30) Shimura, T.; Inoue, M.; Tsujimoto, H.; Sasaki, K.; Iguchi, M., Estimation of wind vector profile using a hexarotor unmanned aerial vehicle and its application to meteorological observation up to 1000 m above surface. *J Atmos Ocean Tech* **2018,** *35*, (8), 1621-1631.
(31) Barbieri, L.; Kral, S. T.; Bailey, S. C. C.; Frazier, A. E.; Jacob, J. D.; Reuder, J.; Brus, D.; Chilson, P. B.; Crick, C.; Detweiler, C.; Doddi, A.; Elston, J.; Foroutan, H.; Gonzalez-Rocha, J.; Greene, B. R.; Guzman, M. I.; Houston, A. L.; Islam, A.; Kemppinen, O.; Lawrence, D.; Pillar-Little, E. A.; Ross, S. D.; Sama, M. P.; Schmale, D. G.; Schuyler, T. J.; Shankar, A.; Smith, S. W.; Waugh, S.; Dixon, C.; Borenstein, S.; de Boer, G., Intercomparison of small unmanned aircraft system (suas) measurements for atmospheric science during the lapse-rate campaign. *Sensors-Basel* **2019,** *19*, (9).
(32) Palomaki, R. T.; Rose, N. T.; van den Bossche, M.; Sherman, T. J.; De Wekker, S. F., Wind estimation in the lower atmosphere using multirotor aircraft. *J Atmos Ocean Tech* **2017,** *34*, (5), 1183-1191.
(33) Neumann, P. P.; Bartholmai, M., Real-time wind estimation on a micro unmanned aerial vehicle using its inertial measurement unit. *Sensors and Actuators A: Physical* **2015,** *235*, 300-310.
(34) Oktay, T.; Eraslan, Y. In *Computational fluid dynamics (cfd) investigation of a quadrotor uav propeller*, International Conference on Energy, Environment and Storage of Energy, 2020; 2020; pp 21-25.
(35) Hedworth, H.; Page, J.; Sohl, J.; Saad, T., Investigating errors observed during uav-based vertical measurements using computational fluid dynamics. *Drones* **2022,** *6*, (9), 253.
(36) Han T, X. C., Liu Y, Yang Y, Zhang Y, Huang Y, Gao X, Zhang X., Bao F, and Li S-M., Application of a new uav measurement methodology to the quantification of co2 and ch4 emissionsfrom a major coking plant. *Atmospheric Measurement Techniques* **2023,** *In Prep*.
(37) Quan, Q., *Introduction to multicopter design and control*. Springer: 2017.

Support Information

A Correction Algorithm for Propeller-Induced Airflow during Three-Dimensional Wind Speed Measurements Made from A Rotary Unmanned Aerial Vehicle

Yanrong Yang[a+], Yuheng Zhang[a+], Tianran Han[a], Conghui Xie[a], Yayong Liu[a], Yufei Huang[a], Jietao Zhou[a], Delong Zhao[b], Xiangyu Gao[c], Shao-Meng Li[a*]

[a] College of Environmental Sciences and Engineering, Peking University, Beijing 100871, China

[b] Beijing Key Laboratory of Cloud, Precipitation and Atmospheric Water Resources, Beijing Meteorological Service, Beijing, China

[c] Beijing Wisdominc Technology Co., Ltd, Beijing, China.

[+] Contributed equally to the work

Correspondence to: Shao-Meng Li (shaomeng.li@pku.edu.cn)

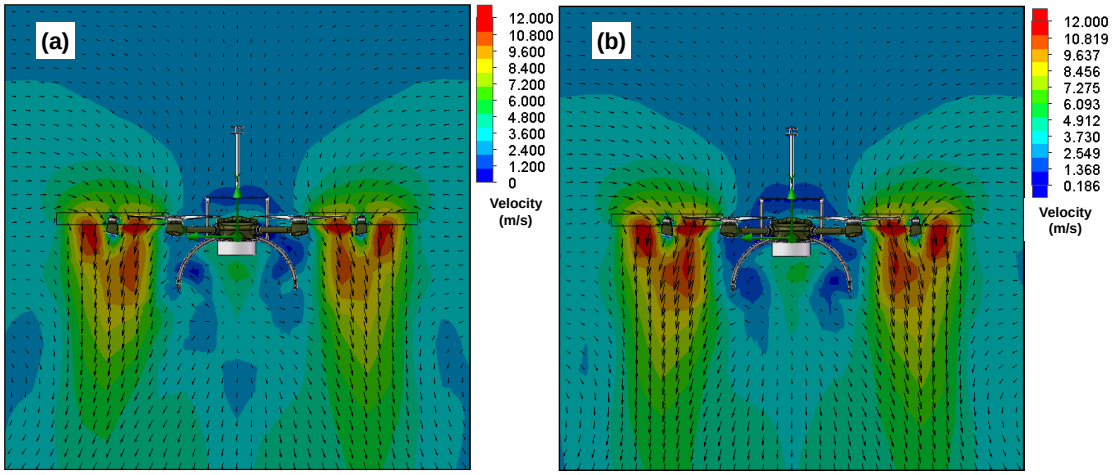

Figure S1. Example results of Computational Fluid Dynamics (CFD) simulation for the unmanned aerial vehicle. (a) and (b) show the flow field simulation for the UAV flying at ground speed of 8m/s with a tailwind speed of 5.4m/s at altitudes of 30 meters and 1000 meters, respectively.

Figure S2. Comparison between UAV-based and Tower-based wind speed measurements.

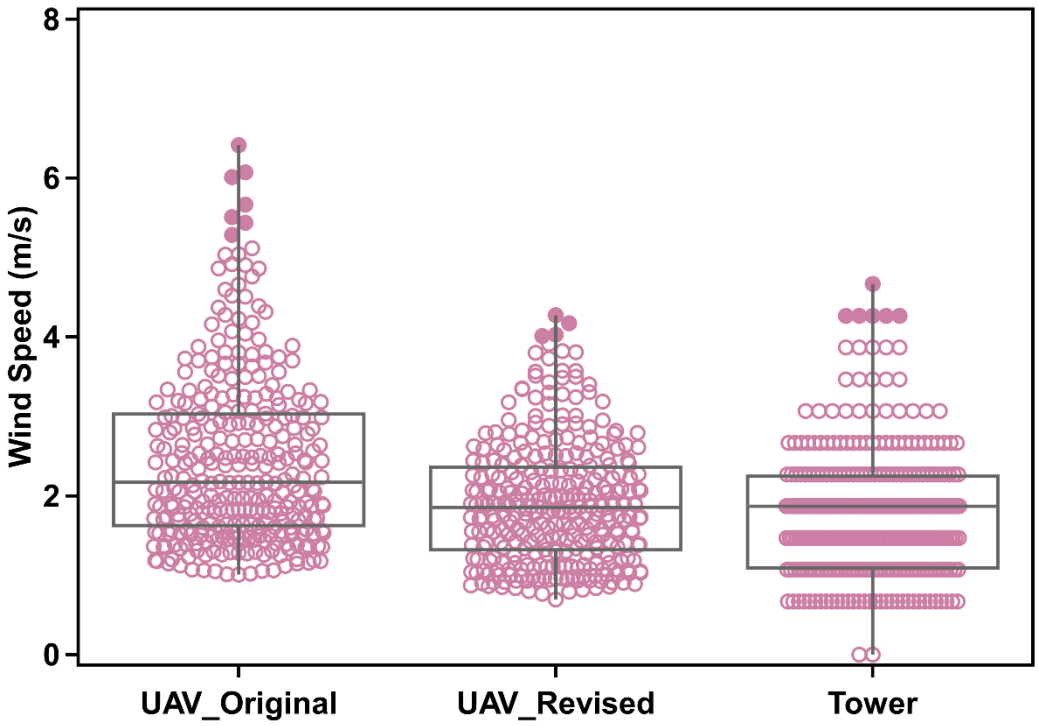

Figure S3. Boxplots of tower-based wind speed (Tower), UAV-based wind speed corrected for motion and attitude (UAV_Original), and UAV-based wind speed with comprehensive correction for rotor disturbance, motion, and attitude (UAV_Revise).

Table S1. Parameters configuration for simulating UAV flight at 30 m altitude.

Wind Direction	Wind Level	Wind Speed	Air Speed	Ground Speed	Attack Angle	Sideslip Angle	Wind Resistance	Pull Force	Theoretical Speed	Corrected Speed
Headwind	1	1.5	19.5	18	11.77	-	58.96	288.99	2633.11	2643.11
	2	3.3	21.3	18	14.51	-	73.23	292.24	2647.85	2658.00
	1	1.5	15.5	14	6.92	-	34.35	284.99	2614.82	2624.82
	2	3.3	17.3	14	8.90	-	44.30	286.36	2621.10	2631.10
	3	5.4	19.4	14	11.63	-	58.23	288.85	2632.44	2642.44
	4	7.9	21.9	14	15.50	-	78.47	293.60	2653.99	2663.99
	1	1.5	11.5	10	3.59	-	17.73	283.47	2607.82	2617.82
	2	3.3	13.3	10	4.92	-	24.35	283.96	2610.08	2620.08
	3	5.4	15.4	10	6.82	-	33.84	284.93	2614.54	2624.54
	4	7.9	17.9	10	9.63	-	48.01	286.96	2623.83	2633.83
	5	10.7	20.7	10	13.56	-	68.23	291.03	2642.36	2652.36
	1	1.5	9.5	8	2.39	-	11.80	283.16	2606.40	2616.40
	2	3.3	11.3	8	3.45	-	17.07	283.43	2607.64	2617.64
	3	5.4	13.4	8	5.00	-	24.76	284.00	2610.24	2620.24
	4	7.9	15.9	8	7.33	-	36.41	285.25	2615.99	2625.99
	5	10.7	18.7	8	10.67	-	53.29	287.89	2628.08	2638.08
Tailwind	1	1.5	16.5	18	7.98	-	39.67	285.68	2617.98	2627.98
	2	3.3	14.7	18	6.14	-	30.45	284.55	2612.78	2622.78

	3	5.4	12.6	18	4.37	-	21.62	283.74	2609.07	2619.07
	4	7.9	10.1	18	2.72	-	13.43	283.23	2606.74	2616.74
	5	10.7	7.3	18	1.38	-	6.82	283.00	2605.65	2615.65
	6	14	4	18	0.41	-	2.00	282.92	2605.30	2615.30
	1	1.5	12.5	14	4.29	-	21.25	283.71	2608.94	2618.94
	2	3.3	10.7	14	3.07	-	15.18	283.32	2607.15	2617.15
	3	5.4	8.6	14	1.94	-	9.58	283.08	2606.02	2616.02
	4	7.9	6.1	14	0.95	-	4.71	282.96	2605.45	2615.45
	5	10.7	3.3	14	0.28	-	1.36	282.92	2605.29	2615.29
	1	1.5	8.5	10	1.89	-	9.34	283.07	2605.98	2615.98
	2	3.3	6.7	10	1.16	-	5.71	282.97	2605.54	2615.54
	3	5.4	4.6	10	0.54	-	2.66	282.93	2605.33	2615.33
	4	7.9	2.1	10	0.11	-	0.55	282.92	2605.27	2615.27
	1	1.5	6.5	8	1.09	-	5.37	282.97	2605.51	2615.51
	2	3.3	4.7	8	0.56	-	2.77	282.93	2605.33	2615.33
	3	5.4	2.6	8	0.17	-	0.84	282.92	2605.28	2615.28
Crosswind	1	1.5	18.06	18	9.76	-0.06	49.05	287.12	2624.55	2634.55
	2	3.3	18.30	18	9.76	0.28	50.61	287.31	2625.42	2635.42
	3	5.4	18.79	18	9.76	0.74	53.93	287.74	2627.37	2637.37
	4	7.9	19.66	18	9.76	1.62	60.12	288.59	2631.28	2641.28
	5	10.7	20.94	18	9.76	3.07	70.20	290.16	2638.42	2648.42
	6	14	22.80	18	9.76	5.51	86.83	293.27	2652.50	2662.50
	1	1.5	14.08	14	5.51	0.06	27.64	284.26	2611.44	2621.44
	2	3.3	14.38	14	5.51	0.28	29.00	284.36	2611.93	2621.93
	3	5.4	15.01	14	5.51	0.74	31.90	284.61	2613.06	2623.06
	4	7.9	16.08	14	5.51	1.62	37.34	285.12	2615.42	2625.42
	5	10.7	17.62	14	5.51	3.07	46.26	286.12	2619.98	2629.98
	6	14	19.80	14	5.51	5.51	61.18	288.23	2629.63	2639.63
	1	1.5	10.11	10	2.66	0.06	13.46	283.23	2606.74	2616.74
	2	3.3	10.53	10	2.66	0.28	14.68	283.29	2606.98	2616.98
	3	5.4	11.36	10	2.66	0.74	17.28	283.42	2607.57	2617.57
	4	7.9	12.74	10	2.66	1.62	22.17	283.71	2608.92	2618.92
	5	10.7	14.65	10	2.66	3.07	30.20	284.34	2611.81	2621.81
	6	14	17.20	10	2.66	5.51	43.73	285.82	2618.60	2628.60
	1	1.5	8.14	8	1.67	0.06	8.54	283.04	2605.86	2615.86
	2	3.3	8.65	8	1.67	0.28	9.70	283.08	2606.02	2616.02
	3	5.4	9.65	8	1.67	0.74	12.20	283.17	2606.43	2616.43
	4	7.9	11.24	8	1.67	1.62	16.89	283.38	2607.42	2617.42
	5	10.7	13.36	8	1.67	3.07	24.60	283.89	2609.74	2619.74
	6	14	16.12	8	1.67	5.51	37.61	285.15	2615.54	2625.54

Table S2. Parameters configuration for simulating UAV flight at 1000 m altitude.

Wind Direction	Wind Level	Wind Speed	Air Speed	Ground Speed	Attack Angle	Sideslip Angle	Wind Resistance	Pull Force	Theoretical Speed	Corrected Speed
Headwind	1	1.5	19.5	18	10.53	-	52.61	287.77	2754.70	2764.70
	2	3.3	21.3	18	12.97	-	65.17	290.32	2766.92	2776.92
	1	1.5	15.5	14	6.22	-	30.85	284.59	2739.47	2749.47
	2	3.3	17.3	14	7.98	-	39.67	285.68	2744.71	2754.71
	3	5.4	19.4	14	10.41	-	51.97	287.65	2754.14	2764.14
	4	7.9	21.9	14	13.85	-	69.78	291.39	2772.01	2782.01
	1	1.5	11.5	10	3.24	-	16.01	283.37	2733.57	2743.57
	2	3.3	13.3	10	4.44	-	21.94	283.77	2735.48	2745.48
	3	5.4	15.4	10	6.13	-	30.40	284.54	2739.24	2749.24
	4	7.9	17.9	10	8.63	-	42.95	286.16	2746.99	2756.99
	5	10.7	20.7	10	12.12	-	60.77	289.37	2762.36	2772.36
	1	1.5	9.5	8	2.16	-	10.68	283.12	2732.36	2742.36
	2	3.3	11.3	8	3.12	-	15.42	283.34	2733.41	2743.41
	3	5.4	13.4	8	4.51	-	22.31	283.79	2735.62	2745.62
	4	7.9	15.9	8	6.59	-	32.68	284.80	2740.45	2750.45
	5	10.7	18.7	8	9.55	-	47.61	286.89	2750.52	2760.52
Tailwind	1	1.5	16.5	18	7.17	-	35.57	285.14	2742.11	2752.11
	2	3.3	14.7	18	5.53	-	27.38	284.24	2737.76	2747.76
	3	5.4	12.6	18	3.94	-	19.50	283.59	2734.62	2744.62
	4	7.9	10.1	18	2.46	-	12.15	283.18	2732.64	2742.64
	5	10.7	7.3	18	1.25	-	6.18	282.98	2731.71	2741.71
	6	14	4	18	0.37	-	1.82	282.92	2731.41	2741.41
	1	1.5	12.5	14	3.88	-	19.17	283.56	2734.51	2744.51
	2	3.3	10.7	14	2.78	-	13.73	283.25	2732.99	2742.99
	3	5.4	8.6	14	1.76	-	8.68	283.05	2732.03	2742.03
	4	7.9	6.1	14	0.87	-	4.28	282.95	2731.54	2741.54
	5	10.7	3.3	14	0.25	-	1.24	282.92	2731.40	2741.40
	1	1.5	8.5	10	1.71	-	8.47	283.04	2732.00	2742.00
	2	3.3	6.7	10	1.05	-	5.18	282.96	2731.61	2741.61
	3	5.4	4.6	10	0.49	-	2.41	282.93	2731.43	2741.43
	4	7.9	2.1	10	0.10	-	0.50	282.92	2731.39	2741.39
	1	1.5	6.5	8	0.99	-	4.87	282.96	2731.59	2741.59
	2	3.3	4.7	8	0.51	-	2.52	282.93	2731.44	2741.44
	3	5.4	2.6	8	0.15	-	0.77	282.92	2731.39	2741.39
Crosswind	1	1.5	18.06	18	8.74	0.05	43.87	286.28	2747.59	2757.59
	2	3.3	18.30	18	8.74	0.25	45.24	286.44	2748.34	2758.34
	3	5.4	18.79	18	8.74	0.68	48.17	286.78	2749.99	2759.99
	4	7.9	19.66	18	8.74	1.47	53.63	287.48	2753.31	2763.31
	5	10.7	20.94	18	8.74	2.78	62.51	288.74	2759.33	2769.33
	6	14	22.80	18	8.74	4.96	77.14	291.21	2771.14	2781.14
	1	1.5	14.08	14	4.96	0.05	24.88	284.00	2736.63	2746.63

2	3.3	14.38	14	4.96	0.25	26.09	284.09	2737.05	2747.05
3	5.4	15.01	14	4.96	0.68	28.67	284.29	2738.02	2748.02
4	7.9	16.08	14	4.96	1.47	33.51	284.71	2740.03	2750.03
5	10.7	17.62	14	4.96	2.78	41.40	285.52	2743.92	2753.92
6	14	19.80	14	4.96	4.96	54.57	287.22	2752.06	2762.06
1	1.5	10.11	10	2.41	0.05	12.18	283.18	2732.64	2742.64
2	3.3	10.53	10	2.41	0.25	13.27	283.22	2732.86	2742.86
3	5.4	11.36	10	2.41	0.68	15.61	283.33	2733.37	2743.37
4	7.9	12.74	10	2.41	1.47	19.99	283.57	2734.52	2744.52
5	10.7	14.65	10	2.41	2.78	27.16	284.08	2736.99	2746.99
6	14	17.20	10	2.41	4.96	39.17	285.27	2742.74	2752.74
1	1.5	8.14	8	1.51	0.05	7.74	283.02	2731.89	2741.89
2	3.3	8.65	8	1.51	0.25	8.79	283.05	2732.03	2742.03
3	5.4	9.65	8	1.51	0.68	11.04	283.12	2732.38	2742.38
4	7.9	11.24	8	1.51	1.47	15.26	283.30	2733.24	2743.24
5	10.7	13.36	8	1.51	2.78	22.16	283.71	2735.22	2745.22
6	14	16.12	8	1.51	4.96	33.74	284.73	2740.14	2750.14

Table S3. Wind speed configuration and simulation results for UAV flight at 30 m altitude.

Wind Direction	Wind Level	Wind Speed	Air Speed	Ground Speed	u_{x_air}	u_{y_air}	u_{z_air}	$u_{x\_sensor\_avg}$	$u_{y\_sensor\_avg}$	$u_{z\_sensor\_avg}$	Δu_{x_avg}	Δu_{x_std}	Δu_{y_avg}	Δu_{y_std}	Δu_{z_avg}	Δu_{z_std}
Headwind	1	1.5	19.5	18	-19.09	0	3.98	-19.74	0.025	-19.737	-0.65	0.0058	0.025	0.015	-2.18	0.024
	2	3.3	21.3	18	-20.62	0	5.34	-20.96	-0.10	-20.965	-0.34	0.26	-0.10	0.061	-2.83	0.16
	1	1.5	15.5	14	-15.39	0	1.87	-15.96	-0.074	-15.961	-0.57	0.13	-0.074	0.0050	-1.44	0.087
	2	3.3	17.3	14	-17.09	0	2.68	-17.76	0.003	-17.757	-0.67	0.042	0.003	0.087	-1.55	0.077
	3	5.4	19.4	14	-19.00	0	3.91	-19.52	0.050	-19.516	-0.51	0.014	0.050	0.0034	-2.13	0.015
	4	7.9	21.9	14	-21.10	0	5.85	-21.64	-0.091	-21.639	-0.54	0.071	-0.091	0.044	-3.18	0.19
	1	1.5	11.5	10	-11.48	0	0.72	-12.20	-0.085	-12.199	-0.72	0.016	-0.085	0.0083	-0.65	0.042
	2	3.3	13.3	10	-13.25	0	1.14	-13.75	-0.11	-13.752	-0.50	0.058	-0.11	0.0085	-1.07	0.078
	3	5.4	15.4	10	-15.29	0	1.83	-15.90	-0.063	-15.903	-0.61	0.15	-0.063	0.0055	-1.46	0.092
	4	7.9	17.9	10	-17.65	0	3.00	-18.24	0.072	-18.242	-0.59	0.067	0.072	0.073	-1.40	0.033
	5	10.7	20.7	10	-20.12	0	4.85	-21.20	-0.029	-21.203	-1.08	0.012	-0.029	0.018	-2.61	0.31
	1	1.5	9.5	8	-9.49	0	0.40	-9.33	-0.0094	-9.328	0.16	0.24	-0.0094	0.026	-0.45	0.069
	2	3.3	11.3	8	-11.28	0	0.68	-11.95	-0.040	-11.950	-0.67	0.0058	-0.040	0.034	-0.60	0.035
	3	5.4	13.4	8	-13.35	0	1.17	-13.86	-0.099	-13.859	-0.51	0.035	-0.099	0.011	-1.09	0.093
	4	7.9	15.9	8	-15.77	0	2.03	-16.48	-0.067	-16.481	-0.71	0.012	-0.067	0.044	-1.47	0.062
	5	10.7	18.7	8	-18.38	0	3.46	-18.71	-0.027	-18.713	-0.34	0.015	-0.027	0.019	-1.82	0.057
Tailwind	1	1.5	16.5	18	-16.34	0.00	2.29	-16.90	0.021	0.81	-0.56	0.015	0.021	0.044	-1.48	0.025
	2	3.3	14.7	18	-14.62	0.00	1.57	-14.92	-0.038	0.24	-0.30	0.018	-0.038	0.017	-1.33	0.030
	3	5.4	12.6	18	-12.56	0.00	0.96	-13.08	-0.042	0.06	-0.52	0.028	-0.042	0.077	-0.90	0.057
	4	7.9	10.1	18	-10.09	0.00	0.48	-10.24	-0.039	-0.10	-0.15	0.021	-0.039	0.045	-0.58	0.066
	5	10.7	7.3	18	-7.30	0.00	0.18	-7.10	-0.070	-0.034	0.19	0.14	-0.070	0.003	-0.21	0.013

	6	14	4	18	-4.00	0.00	0.03	-3.75	-0.055	0.70	0.25	0.047	-0.055	0.010	0.67	0.021
	1	1.5	12.5	14	-12.46	0.00	0.94	-12.94	-0.049	0.015	-0.48	0.065	-0.049	0.028	-0.92	0.065
	2	3.3	10.7	14	-10.68	0.00	0.57	-11.08	0.043	0.12	-0.39	0.028	0.043	0.053	-0.45	0.113
	3	5.4	8.6	14	-8.60	0.00	0.29	-8.26	-0.001	-0.12	0.34	0.027	-0.001	0.045	-0.41	0.063
	4	7.9	6.1	14	-6.10	0.00	0.10	-6.00	-0.067	0.10	0.10	0.013	-0.067	0.013	-0.01	0.065
	5	10.7	3.3	14	-3.30	0.00	0.016	-2.92	-0.041	0.71	0.38	0.054	-0.041	0.003	0.69	0.028
	1	1.5	8.5	10	-8.50	0.00	0.28	-8.20	-0.024	-0.14	0.30	0.063	-0.024	0.047	-0.42	0.054
	2	3.3	6.7	10	-6.70	0.00	0.14	-6.48	-0.058	0.05	0.22	0.066	-0.058	0.011	-0.087	0.027
	3	5.4	4.6	10	-4.60	0.00	0.043	-4.58	0.028	0.68	0.02	0.11	0.028	0.018	0.64	0.135
	4	7.9	2.1	10	-2.10	0.00	0.0041	-1.12	-0.002	0.69	0.98	0.065	-0.002	0.017	0.68	0.015
	1	1.5	6.5	8	-6.50	0.00	0.12	-6.22	-0.063	0.03	0.28	0.057	-0.063	0.014	-0.10	0.028
	2	3.3	4.7	8	-4.70	0.00	0.046	-4.70	-0.025	0.57	0.00	0.030	-0.025	0.029	0.52	0.047
	3	5.4	2.6	8	-2.60	0.00	0.0077	-2.04	0.010	0.70	0.56	0.025	0.010	0.016	0.69	0.018
	1	1.5	18.06	18	-17.80	0.018	3.06	-18.38	-0.04	1.57	-0.58	0.021	-0.062	0.103	-1.49	0.058
	2	3.3	18.30	18	-18.04	0.088	3.10	-18.65	0.18	1.51	-0.62	0.11	0.089	0.016	-1.59	0.043
	3	5.4	18.79	18	-18.52	0.24	3.19	-19.21	0.50	1.65	-0.69	0.075	0.25	0.018	-1.53	0.023
	4	7.9	19.66	18	-19.37	0.56	3.33	-20.21	1.09	1.61	-0.85	0.066	0.53	0.009	-1.72	0.029
	5	10.7	20.94	18	-20.61	1.12	3.55	-21.44	1.76	1.77	-0.83	0.078	0.64	0.024	-1.78	0.041
	6	14	22.80	18	-22.37	2.19	3.86	-23.27	2.60	1.79	-0.90	0.056	0.41	0.046	-2.08	0.038
Crosswind	1	1.5	14.08	14	-14.02	0.014	1.35	-14.35	-0.06	0.17	-0.33	0.12	-0.078	0.012	-1.18	0.063
	2	3.3	14.38	14	-14.32	0.069	1.38	-14.69	-0.01	0.20	-0.38	0.10	-0.084	0.003	-1.18	0.056
	3	5.4	15.01	14	-14.93	0.19	1.44	-15.38	0.31	0.10	-0.44	0.11	0.11	0.025	-1.34	0.080
	4	7.9	16.08	14	-15.99	0.46	1.54	-16.49	0.79	0.16	-0.49	0.14	0.34	0.009	-1.39	0.10
	5	10.7	17.62	14	-17.51	0.94	1.69	-17.78	1.07	0.15	-0.27	0.20	0.13	0.073	-1.54	0.16
	6	14	19.80	14	-19.62	1.90	1.90	-20.04	1.98	0.21	-0.42	0.18	0.082	0.095	-1.69	0.11
	1	1.5	10.11	10	-10.10	0.010	0.47	-10.39	-0.05	-0.065	-0.29	0.11	-0.064	0.021	-0.53	0.042

	2	3.3	10.53	10	-10.52	0.051	0.49	-10.84	0.05	-0.16	-0.32	0.13	0.00	0.075	-0.65	0.094
	3	5.4	11.36	10	-11.35	0.15	0.53	-11.84	0.19	-0.22	-0.49	0.11	0.037	0.017	-0.75	0.16
	4	7.9	12.74	10	-12.73	0.36	0.59	-13.30	0.59	-0.32	-0.57	0.09	0.23	0.023	-0.91	0.15
	5	10.7	14.65	10	-14.61	0.78	0.68	-15.24	0.99	-0.40	-0.63	0.11	0.21	0.011	-1.08	0.15
	6	14	17.20	10	-17.11	1.65	0.80	-17.93	1.71	-0.48	-0.82	0.14	0.056	0.086	-1.28	0.15
	1	1.5	8.14	8	-8.14	0.0080	0.24	-7.83	-0.06	-0.19	0.31	0.15	-0.065	0.047	-0.43	0.015
	2	3.3	8.65	8	-8.65	0.042	0.25	-8.44	-0.05	-0.18	0.21	0.22	-0.094	0.085	-0.43	0.053
	3	5.4	9.65	8	-9.65	0.13	0.28	-9.58	0.11	-0.25	0.07	0.15	-0.011	0.025	-0.53	0.033
	4	7.9	11.24	8	-11.23	0.32	0.33	-11.32	0.35	-0.38	-0.09	0.17	0.030	0.0081	-0.71	0.035
	5	10.7	13.36	8	-13.34	0.72	0.39	-13.52	0.44	-0.32	-0.19	0.20	-0.28	0.066	-0.71	0.088
	6	14	16.12	8	-16.04	1.55	0.47	-16.33	1.94	-0.45	-0.29	0.29	0.40	0.050	-0.92	0.047

Table S4. Wind speed configuration and simulation results for UAV flight at 1000 m altitude.

Wind Direction	Wind Level	Wind Speed	Air Speed	Ground Speed	u_{x_air}	u_{y_air}	u_{z_air}	$u_{x\_sensor\_avg}$	$u_{y\_sensor\_avg}$	$u_{z\_sensor\_avg}$	Δu_{x_avg}	Δu_{x_std}	Δu_{y_avg}	Δu_{y_std}	Δu_{z_avg}	Δu_{z_std}
Headwind	1	1.5	19.5	18	-19.17	0.00	3.98	-19.61	-0.064	1.71	-0.52	0.037	-0.064	0.046	-2.27	0.062
	2	3.3	21.3	18	-20.76	0.00	5.34	-21.73	-0.069	2.07	-1.11	0.17	-0.069	0.023	-3.27	0.28
	1	1.5	15.5	14	-15.41	0.00	1.87	-15.77	-0.045	0.29	-0.38	0.13	-0.045	0.017	-1.58	0.027
	2	3.3	17.3	14	-17.13	0.00	2.68	-17.68	-0.016	0.86	-0.59	0.13	-0.016	0.019	-1.82	0.025
	3	5.4	19.4	14	-19.08	0.00	3.91	-19.63	0.018	1.74	-0.63	0.017	0.018	0.013	-2.17	0.072
	4	7.9	21.9	14	-21.26	0.00	5.85	-22.38	-0.049	2.54	-1.28	0.043	-0.049	0.012	-3.31	0.33
	1	1.5	11.5	10	-11.48	0.00	0.72	-11.97	-0.049	-0.15	-0.49	0.12	-0.049	0.088	-0.87	0.14
	2	3.3	13.3	10	-13.26	0.00	1.14	-13.71	-0.033	0.10	-0.46	0.041	-0.033	0.0093	-1.04	0.039
	3	5.4	15.4	10	-15.31	0.00	1.83	-15.64	-0.046	0.25	-0.35	0.11	-0.046	0.026	-1.58	0.049
	4	7.9	17.9	10	-17.70	0.00	3.00	-18.44	-0.060	0.93	-0.79	0.048	-0.060	0.059	-2.06	0.054

	5	10.7	20.7	10	-20.24	0.00	4.85	-21.07	0.024	2.05	-0.94	0.0094	0.024	0.0089	-2.81	0.029
	1	1.5	9.5	8	-9.49	0.00	0.40	-9.26	-0.034	-0.12	0.23	0.21	-0.034	0.058	-0.52	0.036
	2	3.3	11.3	8	-11.28	0.00	0.68	-11.88	0.000	-0.092	-0.60	0.14	0.000	0.055	-0.77	0.069
	3	5.4	13.4	8	-13.36	0.00	1.17	-13.71	-0.094	0.12	-0.36	0.017	-0.094	0.012	-1.05	0.020
	4	7.9	15.9	8	-15.79	0.00	2.03	-16.28	-0.074	0.39	-0.51	0.025	-0.074	0.016	-1.64	0.018
	5	10.7	18.7	8	-18.44	0.00	3.46	-19.05	0.045	1.60	-0.67	0.039	0.045	0.048	-1.86	0.0092
Tailwind	1	1.5	16.5	18	-16.37	0.00	2.06	-16.90	-0.028	0.60	-0.56	0.0016	-0.028	0.031	-1.46	0.051
	2	3.3	14.7	18	-14.63	0.00	1.42	-15.10	-0.12	0.23	-0.49	0.010	-0.12	0.019	-1.18	0.0088
	3	5.4	12.6	18	-12.57	0.00	0.87	-13.39	-0.083	0.09	-0.83	0.0037	-0.083	0.011	-0.77	0.0050
	4	7.9	10.1	18	-10.09	0.00	0.43	-9.85	0.014	0.02	0.24	0.0057	0.014	0.013	-0.41	0.017
	5	10.7	7.3	18	-7.30	0.00	0.16	-6.95	-0.047	0.00	0.35	0.0004	-0.047	0.021	-0.16	0.0035
	6	14	4	18	-4.00	0.00	0.026	-3.72	-0.024	0.78	0.28	0.028	-0.024	0.002	0.75	0.0057
	1	1.5	12.5	14	-12.47	0.00	0.84	-13.25	-0.072	0.07	-0.79	0.025	-0.072	0.027	-0.78	0.049
	2	3.3	10.7	14	-10.69	0.00	0.52	-10.98	-0.079	-0.19	-0.29	0.0028	-0.079	0.031	-0.71	0.071
	3	5.4	8.6	14	-8.60	0.00	0.26	-8.24	-0.058	-0.16	0.35	0.0091	-0.058	0.007	-0.42	0.013
	4	7.9	6.1	14	-6.10	0.00	0.092	-6.07	-0.021	0.27	0.03	0.0035	-0.021	0.018	0.18	0.025
	5	10.7	3.3	14	-3.30	0.00	0.014	-2.83	-0.034	0.73	0.47	0.030	-0.034	0.003	0.72	0.0037
	1	1.5	8.5	10	-8.50	0.00	0.25	-8.12	-0.056	-0.20	0.38	0.013	-0.056	0.005	-0.45	0.030
	2	3.3	6.7	10	-6.70	0.00	0.12	-6.54	-0.052	0.10	0.16	0.017	-0.052	0.011	-0.019	0.0091
	3	5.4	4.6	10	-4.60	0.00	0.04	-4.50	-0.017	0.69	0.10	0.071	-0.017	0.042	0.65	0.000
	4	7.9	2.1	10	-2.10	0.00	0.0037	-1.24	-0.0082	0.75	0.86	0.049	-0.0082	0.0019	0.75	0.0016
	1	1.5	6.5	8	-6.50	0.00	0.11	-6.38	0.0086	0.13	0.12	0.0050	0.0086	0.0068	0.02	0.0028
	2	3.3	4.7	8	-4.70	0.00	0.042	-4.60	0.0092	0.68	0.10	0.0088	0.0092	0.039	0.63	0.028
	3	5.4	2.6	8	-2.60	0.00	0.0070	-2.00	0.0013	0.77	0.60	0.051	0.0013	0.0055	0.76	0.010
Crosswind	1	1.5	18.06	18	-17.85	0.02	2.75	-18.50	-0.088	0.66	-0.65	0.033	-0.10	0.031	-2.09	0.021
	2	3.3	18.30	18	-18.09	0.08	2.78	-18.87	0.11	0.64	-0.78	0.008	0.027	0.0057	-2.14	0.030

3	5.4	18.79	18	-18.57	0.22	2.86	-19.49	0.44	0.59	-0.91	0.027	0.21	0.069	-2.27	0.021
4	7.9	19.66	18	-19.42	0.51	2.99	-20.34	0.76	0.67	-0.91	0.048	0.25	0.041	-2.32	0.027
5	10.7	20.94	18	-20.67	1.02	3.18	-21.64	1.13	0.66	-0.97	0.018	0.12	0.025	-2.52	0.0079
6	14	22.80	18	-22.45	1.97	3.47	-23.56	2.09	0.76	-1.10	0.019	0.12	0.026	-2.70	0.037
1	1.5	14.08	14	-14.03	0.01	1.22	-14.27	-0.089	0.18	-0.25	0.016	-0.10	0.037	-1.04	0.013
2	3.3	14.38	14	-14.33	0.06	1.24	-14.63	-0.037	0.062	-0.30	0.014	-0.10	0.0029	-1.18	0.0080
3	5.4	15.01	14	-14.95	0.18	1.30	-15.22	0.16	0.37	-0.27	0.14	-0.01	0.12	-0.93	0.42
4	7.9	16.08	14	-16.01	0.41	1.39	-16.61	0.48	0.42	-0.60	0.28	0.068	0.064	-0.97	0.78
5	10.7	17.62	14	-17.53	0.85	1.52	-18.02	1.28	0.078	-0.49	0.030	0.42	0.12	-1.45	0.031
6	14	19.80	14	-19.65	1.71	1.71	-20.00	1.68	0.084	-0.35	0.10	-0.036	0.23	-1.63	0.070
1	1.5	10.11	10	-10.10	0.01	0.42	-9.84	-0.026	-0.09	0.26	0.094	-0.035	0.078	-0.51	0.067
2	3.3	10.53	10	-10.52	0.05	0.44	-10.35	-0.049	-0.17	0.17	0.036	-0.10	0.047	-0.61	0.088
3	5.4	11.36	10	-11.35	0.13	0.48	-11.23	0.16	-0.25	0.12	0.047	0.028	0.028	-0.73	0.018
4	7.9	12.74	10	-12.73	0.33	0.54	-12.52	0.24	-0.27	0.21	0.081	-0.093	0.086	-0.81	0.022
5	10.7	14.65	10	-14.62	0.71	0.62	-14.34	0.83	-0.38	0.27	0.15	0.12	0.11	-1.00	0.044
6	14	17.20	10	-17.13	1.49	0.72	-17.18	1.45	-0.60	-0.05	0.10	-0.037	0.25	-1.32	0.14
1	1.5	8.14	8	-8.14	0.01	0.21	-7.96	-0.073	-0.071	0.17	0.003	-0.080	0.0092	-0.29	0.014
2	3.3	8.65	8	-8.65	0.04	0.23	-8.53	-0.14	-0.12	0.12	0.070	-0.17	0.073	-0.35	0.075
3	5.4	9.65	8	-9.65	0.11	0.25	-9.69	0.019	-0.17	-0.044	0.018	-0.10	0.044	-0.42	0.059
4	7.9	11.24	8	-11.24	0.29	0.30	-11.46	0.19	-0.27	-0.22	0.0078	-0.10	0.014	-0.57	0.010
5	10.7	13.36	8	-13.34	0.65	0.35	-13.68	0.58	-0.29	-0.34	0.044	-0.063	0.21	-0.64	0.051
6	14	16.12	8	-16.06	1.40	0.43	-16.69	1.30	-0.22	-0.64	0.0080	-0.094	0.023	-0.65	0.021